THE ASTROPHYSICAL JOURNAL, 409:275–281, 1993 May 20

DETECTION OF MAGNETOHYDRODYNAMIC SHOCKS IN THE L1551 OUTFLOW

M. BARSONY
Harvard-Smithsonian Center for Astrophysics, MS-78, 60 Garden Street, Cambridge, MA 02138
AND
N. Z. SCOVILLE AND C. J. CHANDLER
Owens Valley Radio Observatory, California Institute of Technology 105-24, Pasadena, CA 91125
Received 1992 August 10; accepted 1992 November 10

ABSTRACT

We report the results of CO $J = 1 \rightarrow 0$ mapping of portions of the blue outflow lobe of L1551 with $\sim 7''$ (N–S) $\times$ $4''$ (E–W) resolution, obtained with the three-element OVRO millimeter array. Comparison of our interferometer mosaic with lower resolution single-dish data shows that we resolve the strongest single-dish emission regions into filamentary structures, such as are characteristic of shock fronts mapped via their near-infrared H_2 emission in other outflow sources.

We detect a continuous velocity gradient across the brightest filamentary structure in our maps. The projected, deconvolved, FWHM of this feature is 1–2 $\times$ 10^{16} cm, similar to that predicted in theoretical models of C-shocks. Combined with the velocity gradient, this suggests that the emission originates from within a magnetohydrodynamic shock front, possibly resulting from the interaction of a stellar wind with dense, ambient material. In contrast, the discontinuous J-shocks expected in regions with low or no magnetic field should have a thickness $\leq 10^{15}$ cm, which would be unresolved at our spatial resolution. Based on the shock models of Draine and coworkers, the magnetic field strengths required to account for the structure are in the range 10–30 μG. We suggest future high spatial resolution mapping of this feature in its near-infrared CO and H_2 emission, to characterize further the temperature and density structure of the neutral gas within the shock.

Subject headings: ISM: individual (L1551) — ISM: jets and outflows — MHD — radio lines: ISM — shock waves — techniques: interferometric

1. INTRODUCTION

The bipolar outflow in L1551 subtends the largest solid angle ($10' \times 30'$) of any molecular outflow. Its large angular extent, coupled with its proximity ($d = 140$ pc), makes it the best candidate for detailed studies of outflow structure. Since its discovery (Snell, Loren, & Plambeck 1980), the L1551 ouflow has been mapped with single-aperture telescopes in the lowest rotational transition of CO with increasingly better spatial resolution. The most dramatic finding of these studies is the striking shell-like morphology of the blue outflow lobe (Snell & Schloerb 1985; Moriarty-Schieven et al. 1987; Uchida et al. 1987; Rainey et al. 1987; Moriarty-Schieven & Snell 1988; Fridlund et al. 1989). The highest radial velocities are found along the axis of the blue outflow lobe, with progressively lower radial velocities at larger perpendicular distances from the outflow axis.

IRAS was able to resolve the L1551 outflow even at 60 μm and 100 μm, because of its large angular extent (twice the CO size) in the far-IR. The far-IR luminosity emanating from the outflow lobes is considerable, amounting to nearly 50% of the bolometric luminosity of the source powering the outflow, the embedded object, L1551/IRS 5 (Edwards et al. 1986; Clark et al. 1986). The dust responsible for the observed far-IR emission must be shock-heated, based on the spatial distribution of its emission intensity (Edwards et al. 1986).

Early observations by Snell et al. (1980) showed that the observed high-velocity molecular material must consist of ambient cloud gas, swept up by a stellar wind originating from L1551/IRS 5. Optical HH objects, and later, the optical/radio jet observed to emanate from IRS 5, provided direct evidence for the presence of this otherwise unseen stellar wind. However, the relationship between the radio/optical jet emanating from L1551/IRS 5 and the much larger scale outflow lobes observed in the emission from cold, molecular gas has remained elusive. The estimated mass of ionized gas in the radio jets is between 0.4 and 8 $\times$ 10^{-6} $M_\odot$ (Snell et al. 1985). The best estimate for the momentum of the radio jets of IRS 5, assuming a jet velocity of 450 km s^{-1} (see Stocke et al. 1988), is therefore 1.8 $\times$ 10^{-4} to 3.6 $\times$ 10^{-3} $M_\odot$ km s^{-1}, whereas the momentum in the cold molecular gas is 15.6 $M_\odot$ km s^{-1} (Moriarty-Schieven & Snell 1988).

It has been suggested that the missing momentum could be supplied by an *atomic* wind component. However, there is no conclusive evidence for the presence of a collimated H I wind in the L1551 outflow. Although extremely high-velocity (± 180 km s^{-1}) H I toward L1551 has been detected by several workers (Lizano et al. 1988; Barsony, Yun, & Stark 1993) it turns out that such high velocities in H I gas are present over many square degrees of sky toward the L1551 region, encompassing the entire outflow area (Stark et al. 1992). In addition, searches for high-velocity H I emission from molecular outflow sources have been disappointing. In the few instances such H I emission has been mapped (DR 21, Russel et al. 1992; HH 7–11, Rodriguez et al. 1990; NGC 2071, Bally & Stark 1983), the maps are consistent with the H I being more closely associated with the molecular outflow component, rather than forming a separate, more highly collimated wind component.

Discrete short periods of high mass loss from L1551/IRS 5 could solve the momentum problem for the case of this outflow. From a detailed spectroscopic study of the HH objects in the L1551 outflow, the derived time scale between major mass-loss outbursts is estimated to be ≈ 1000 yr (Stocke

et al. 1988), whereas the molecular outflow lifetime is 10^5 yr (Moriarty-Schieven & Snell 1988). It would require seven outbursts each of 50 yr duration and a mass-loss rate of $10^{-4}\ M_\odot\ \mathrm{yr}^{-1}$ (for example, in an FU Orionis event) to provide the observed 15.6 km s^{-1} of momentum in the L1551 outflow lobes, assuming a wind velocity of 450 km s^{-1}.

In order to study the gasdynamics of the blue outflow lobe at small scales, and to resolve any possible shock structures, we undertook mapping of the brightest single-dish emission peaks at high angular resolution (7″ × 4″) with the Owens Valley Radio Observatory's millimeter-wave interferometer. The observations and data reduction methods are described in § 2, the results and discussion are presented in §§ 3 and 4, respectively, and the conclusions are summarized in § 5.

2. OBSERVATIONS AND DATA REDUCTIONS

The Owens Valley Radio Observatory's three-element millimeter interferometer was used to make ^{12}CO $J = 1 \rightarrow 0$ observations of 20 positions in the blue (southwestern) outflow lobe of L1551 in 1986 October and November. The typical total on-source integration time at each position was 4 hr, and the noise level was 0.3 Jy beam^{-1} in each 1 MHz channel. The spectral resolution was 2.6 km s^{-1} (1 MHz) using a 32 channel filterbank covering 83 km s^{-1}. The synthesized beam was ~7″ N–S × 4″ E–W, although its actual value varied slightly with pointing center, as listed in Table 1. The primary beam size at this frequency is 63″. The primary amplitude calibrator was W3(OH), which has a flux of 4.0 Jy at 115 GHz. The phase calibrator was 0420−014.

During each 12 hr track, 10 positions were observed sequentially for 2 minutes each, followed by the phase calibrator for 5 minutes. This procedure allowed for 15 such sequences per track, or roughly 30 minutes on-source integration at each position per track. The 20 observed positions are listed in Table 1 as offsets in arcminutes from the (0, 0) position corresponding to $\alpha_{1950} = 04^h28^m40^s.6$, $\delta_{1950} = 18°01'49''$. The 20 observed positions were divided into two sets of 10 positions, which we will refer to as fields 1 and 2. The 10 positions in each field were partially overlapped with half-beam spacing. Each field was observed twice per configuration. In the second observation of a field in each configuration, the time at which each position in the field was observed was shifted by 15 minutes relative to the previous night's time of observation in order to maximize the UV coverage at each of the 20 positions.

TABLE 1

POINTING CENTERS AND SYNTHESIZED BEAMS OF INTERFEROMETER FIELDS IN L1551 BLUE LOBE

Position	R.A. Offset	Decl. Offset	Beam FWHM	Beam P.A.
Field 1:				
Position 1	0′	0′	6″.4 × 4″.1	0°.2
Position 2	−1.1	−1.3	6.8 × 3.9	−2.4
Position 3	−1.2	−4.0	6.9 × 4.0	−1.0
Position 4	−1.8	−4.2	7.3 × 3.9	−0.3
Position 5	−1.68	−3.62	7.0 × 3.9	2.3
Position 6	−2.18	−3.18	6.9 × 4.0	1.5
Position 7	−2.30	−3.80	7.6 × 4.2	3.0
Position 8	−2.80	−3.40	7.7 × 4.2	2.8
Position 9	−2.68	−2.80	7.6 × 4.2	2.0
Position 10	−3.18	−2.90	7.6 × 4.2	1.2
Field 2:				
Position 1	0	0	6″.4 × 4″.1	0°.2
Position 2	−0.5	−0.4	7.6 × 3.8	−1.1
Position 3	−1.1	−0.6	7.9 × 3.7	1.0
Position 4	−1.7	−0.7	7.7 × 3.8	1.0
Position 5	−2.3	−0.8	7.6 × 3.8	1.2
Position 6	−2.9	−0.9	7.9 × 3.8	1.2
Position 7	−3.5	−1.0	7.8 × 3.8	2.4
Position 8	−4.1	−1.1	7.7 × 3.7	3.1
Position 9	−4.2	−1.4	7.5 × 3.7	1.7
Position 10	−4.8	−1.4	7.4 × 3.7	2.6

NOTE.—Offsets are from the (0, 0) position of: $\alpha_{1950} = 04^h28^m40^s.6$, $\delta_{1950} = 18°01'49''$. This is 0^s.4 east and 8″ north of the position of L1551/IRS 5.

Uniformly weighted maps of all channels at each position were created using the MX routine in AIPS. The positions comprising each field were corrected for the OVRO primary beam response, and mosaicked together. The noise level at the edge of each primary beam is thus increased, and this nonuniformity in the noise has been kept in mind when interpreting the final maps.

The integrated CO emission shown in Figures 1 and 2 was produced using a masking technique. The original channel maps were first smoothed by a Gaussian with 3 times worse resolution than the original synthesized beam. A mask was prepared from the resulting smoothed maps, such that all emission at a level below 2.5 σ in each map was set to zero, and all regions with positive emission at a level $\geq 2.5\ \sigma$ were set to unity. The original data were then multiplied by this mask before producing the zero-moment maps. We present the integrated emission observed by the interferometer in this way, since negative bowls flanking positive emission regions are present in the original CLEANed channel maps. Such negative bowls are caused by the presence of extended emission on scales larger than can be directly detected by the interferometer.

3. RESULTS

Figure 1 shows an overlay of the integrated ^{12}CO $J = 1 \rightarrow 0$ emission detected by the interferometer on an optical image of the region. The optical CCD image was taken through a narrow-band filter which transmits Hα and [N II] emission lines tracing shocked gas. The brightest, most extended optical nebulosity is HH 102. The bright, nebulous emission knot in the southwestern corner of the image is HH 28. The outflow source, L1551/IRS 5, is located at $\alpha_{1950} = 04^h28^m40^s.1$, $\delta_{1950} = 18°01'41''$. The resolution of the optical image is 1″.5, only a factor of ≈2 better in the E–W direction than the resolution of the OVRO CO map.

All the positions we mapped with the interferometer, with the exception of the one centered on IRS 5, are in the blue outflow lobe of the L1551 molecular outflow as previously mapped by single-dish studies. Figure 1 encompasses less than half of the entire extent of the blue outflow lobe. The interferometer map shown in Figure 1 was produced by integrating the emission over seven velocity channels, covering the velocity range $-1.2\ \mathrm{km\ s^{-1}} \leq V_{\mathrm{LSR}} \leq 14.8\ \mathrm{km\ s^{-1}}$. The flux cutoff in each channel map was 2.5 σ (corresponding to 2.2 Jy beam^{-1} km s^{-1}), so that only positive emission above this level in each velocity channel was included in the integration.

Figure 1 shows that at high spatial resolution, the CO emission breaks up into filamentary structures, morphologically similar to the shock structures seen in the optical. The strongest CO feature in our map, located between $04^h28^m20^s.8 \leq \alpha_{1950} \leq 04^h28^m25^s.1$ and $17°59'43'' \leq \delta_{1950} \leq 18°01'19''$, corresponds very well with a lane of obscuration at this location, as

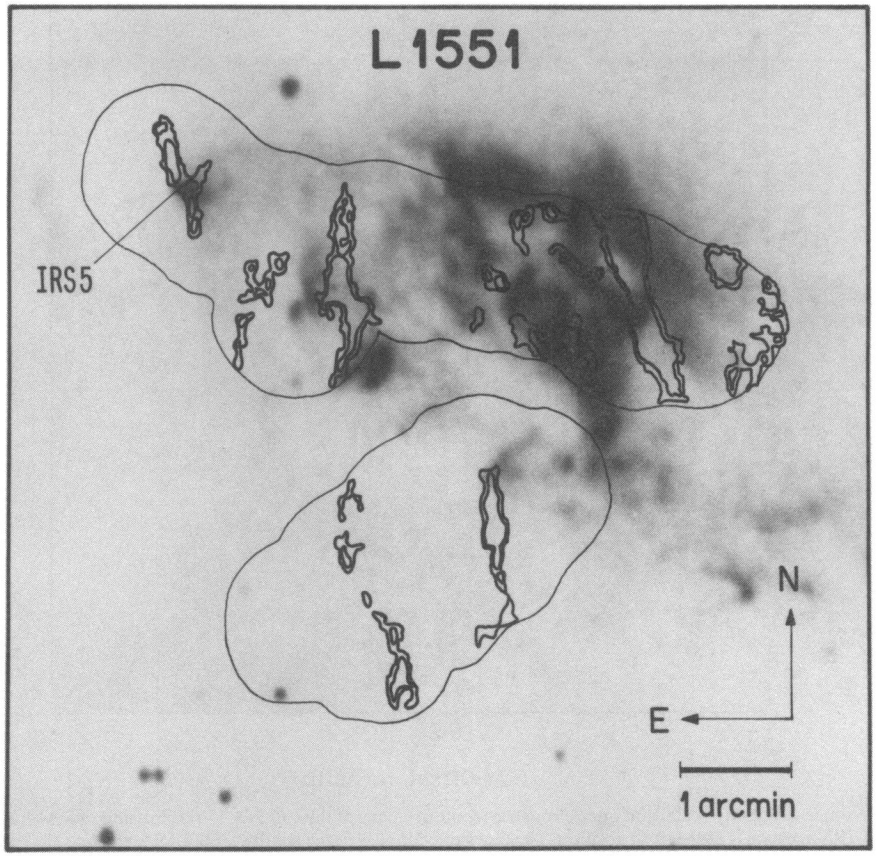

FIG. 1.—Integrated CO $J = 1 \rightarrow 0$ emission detected by the OVRO interferometer, superposed on the narrow-band Hα and [N II] CCD image of the inner 10′ × 10′ region of the L1551 outflow (from Graham & Heyer 1990). The blueshifted portion of the molecular outflow lies to the west of the exciting source, L1551/IRS 5, indicated in the figure. The thin black contour outlines the 20 overlapping 1′ diameter positions mapped with the interferometer. The contours are at 3% and 5% of the peak (14.6 Jy beam^{-1} km s^{-1}) value of the integrated CO emission, outlining the regions masked.

well as with an emission peak previously seen in single-dish maps (e.g., Moriarty-Schieven & Snell 1988). It also coincides with the location of "feature B," a source previously detected via lunar occultation observations and deduced to have a source size less than 10″ along the Moon's path (see Snell & Schloerb [1985]; although note that the coordinates of "feature A" and "feature B" are interchanged in this reference). We discuss the properties of this feature in more detail below.

Figure 2 shows the emission detected with the interferometer overlaid on the gray-scale single-dish map (Moriarty-Schieven & Snell 1988) of part of the blue outflow lobe and a small part of the redshifted lobe. The redshifted lobe is to the northeast of L1551/IRS 5, whereas the blueshifted outflow lobe, which is where most of the OVRO mapping was carried out, is to the southwest. The single-dish data represented in gray scale were integrated over the velocity intervals -1 km s$^{-1} \leq V_{\rm LSR} \leq +5$ km s^{-1} *and* 8 km s$^{-1} \leq V_{\rm LSR} \leq 14$ km s^{-1}. This spans the entire velocity range over which the interferometer detected CO emission, excepting the cloud rest velocities (5 km s$^{-1} \leq V_{\rm LSR} \leq 8$ km s^{-1}), which would confuse the single-dish image. White corresponds to lack of emission, whereas darker areas correspond to stronger emission regions. The gray-scale pixels are 12″ square. Although the single-dish observations were made with a 45″ FWHM Gaussian beam, the map was processed using a maximum entropy deconvolution algorithm (MEM). The best resolution (≈20″) is attained only at map positions with the highest signal-to-noise ratio, still a factor of 3 worse than the interferometer's N–S resolution, and a factor of 6 worse than its E–W resolution. The contours show the CO emission detected by the interferometer integrated over the range -1 km s$^{-1} \leq V_{\rm LSR} \leq 14$ km s^{-1}. No CO emission at radial velocities higher than ±8 km s^{-1} away from line center ($V_{\rm LSR} = 6.5$ km s^{-1}) was detected in the OVRO data, although we tried to enhance our sensitivity to such emission by averaging the UV data over four channels at a time (corresponding to 10.6 km s^{-1} intervals) before making maps.

There is generally good spatial correspondence between the single-dish CO emission and the interferometer maps, in the sense that the regions of strong emission in the low-resolution data are also those with associated CO emission when viewed with the interferometer. At high resolution, the emission is seen to comprise numerous filamentary clumps. Where the emission is sufficiently extended that it covers more than one observed position, it was detected in multiple, independent overlapping fields.

No CO $J = 1 \rightarrow 0$ emission was detected by the interferometer over much of the observed area. Generally, the emission-free regions in the interferometer map correspond to the areas of low surface brightness in the single-dish map. This lack of emission indicates that the gas in such regions may be smoothly distributed over large scales, since the interferometer is sensi-

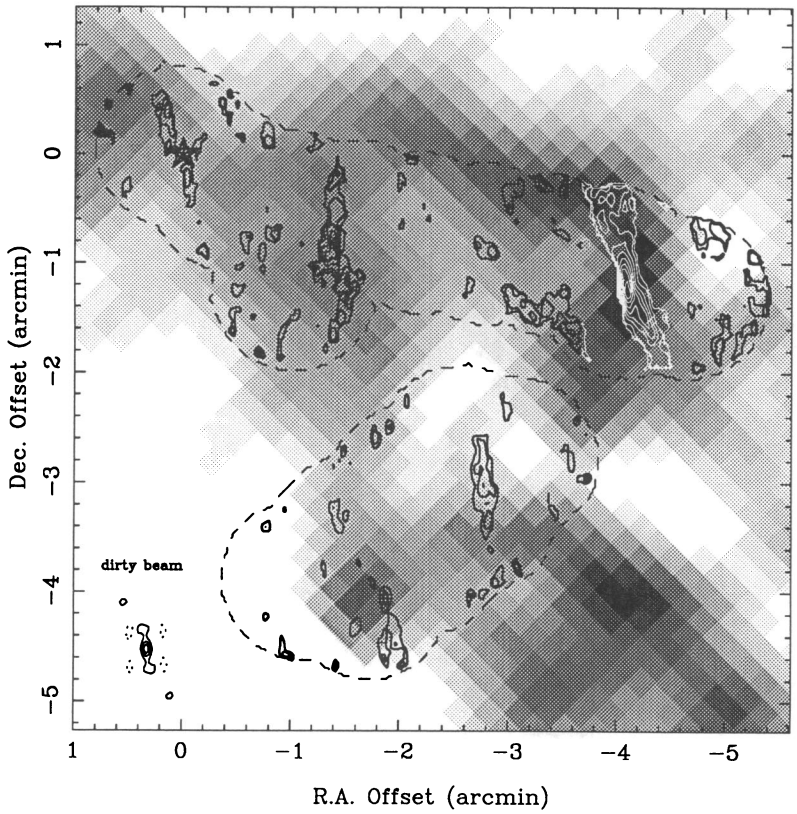

FIG. 2.—A comparison of the single-dish (gray-scale) and interferometric (contour) maps of the CO $J = 1 \rightarrow 0$ emission in the blue lobe of the L1551 outflow. The star marks the position of L1551/IRS 5, which is at the (0, 0) position. The blueshifted lobe is to the southwest of IRS 5, whereas the redshifted lobe is to the northeast. The region mapped by the OVRO interferometer is outlined by the dashed lines. The resolution over the entire OVRO map is $\approx 7''$ (N–S) $\times$ $4''$ (E–W), with the dirty beam indicated in the lower left corner. The contour levels of the dirty beam are at -15%, 15%, 45%, and 75% of the peak value of unity. The integrated CO emission is contoured at 5%, 12.5%, 25%, 37.5%, 50%, 62.5%, 75%, 87.5%, and 100% of the peak value of 14.6 Jy beam^{-1} km s^{-1}.

tive only to small-scale structures, resolving out structures $\geq 30''$.

Figure 3 shows the channel maps of the brightest CO filament detected by the interferometer, progressing from the cloud rest velocity (6.5 km s^{-1} V_{LSR}), to progressively bluer velocities. The positional shift of this feature with velocity is most clearly illustrated in Figure 3*d*. Here, we have superposed the 3 σ contours of this feature as seen at each velocity on each other.

Figure 4 shows the first moment map of the strongest coherent region of CO $J = 1 \rightarrow 0$ emission. A systematic radial velocity gradient is detected across this feature at a position angle of 140°, spanning the velocity range 1.0 km s^{-1} $\leq V_{LSR} \leq +8$ km s^{-1}. (The cloud rest velocity is at $V_{LSR} = 6.5$ km s^{-1}.) The most blueshifted gas is closer to the exciting source, L1551/IRS 5, while the most redshifted gas is farthest away. This feature is well-resolved spatially by the OVRO observations, ranging 3–5 beams in extent E–W and greater than 8 beams N–S. Its total width varies between $12''$ and $21''$, corresponding to 2–3 $\times$ 10^{16} cm at the source.

Within the area $04^h28^m20^s.8 \leq \alpha_{1950} \leq 04^h28^m25^s.1$, $17°59'43'' \leq \delta_{1950} \leq 18°01'19''$, where we detect the strongest CO emission with the interferometer, only 33% of the single-dish flux (767 Jy km s^{-1}) is recovered. This estimate was made by assuming a conversion factor of 22 Jy K^{-1} in the $45''$ FWHM Gaussian beam of the FCRAO (Five College Radio Astronomy Observatory) antenna, and integrating the single-dish flux over the same area and velocity interval over which we integrated the flux detected by the interferometer.

4. DISCUSSION

4.1. CO *Morphology*

The features in Figure 2 are all well-resolved by our observations and lie roughly perpendicular to the direction of the blue outflow lobe seen in single-dish maps. Figure 1 shows that the features we detect coincide with a region found by Graham & Heyer (1990) to be the origin of shock-excited Hα and [N II] line emission. The brightest CO emission is located along lanes of obscuration in those optical images, suggesting that the molecular gas lies in front of the shocked material evident from its emission lines. The presence of shocked gas in the vicinity of the CO makes it likely that the material giving rise to the CO emission is also shocked. These filamentary structures may either be the consequence of successive outburst events from IRS 5 (as alluded to in the Introduction) or the result of the wind from IRS 5 interacting with preexisting inhomogeneities in the ambient cloud.

The brightest feature depicted in Figures 3 and 4 displays a velocity gradient across its entire length. In a picture in which the CO filaments are shocked, as suggested by the proximity of the optical tracers of shock activity, this velocity gradient could be caused by the impact of the stellar wind responsible for the large-scale outflow with ambient clumps. The velocity

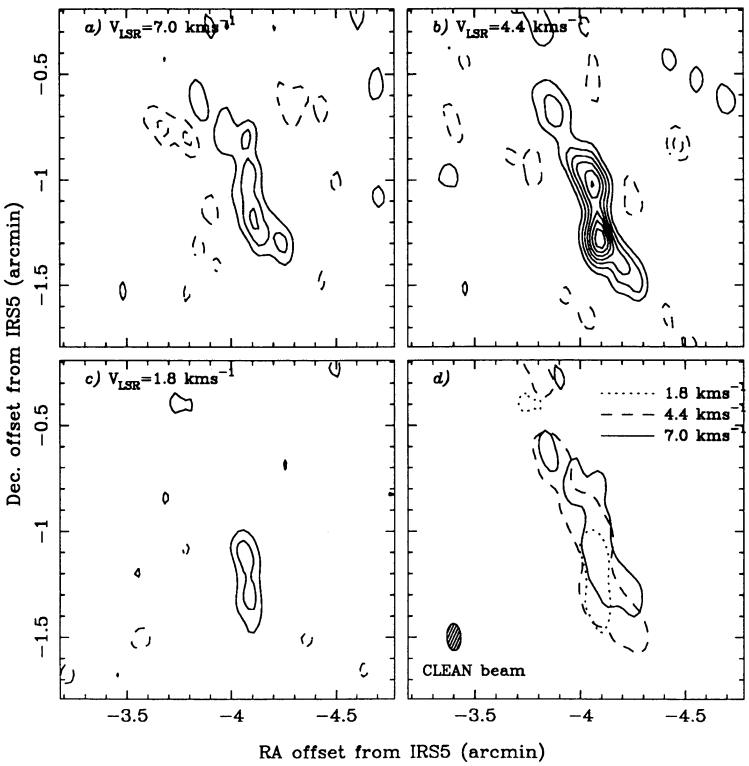

FIG. 3.—Maps of the individual 1 MHz channels containing emission from the brightest CO filament in Fig. 2. Contours are evenly spaced at 3 σ intervals of 1 Jy beam^{-1} in all the maps. The center LSR velocity is marked in each panel. Fig. 3*d* shows the 3 σ contour of the filament in all three channels overlaid, demonstrating the dependence on velocity of the position of the feature. The 50% contour of the synthesized clean beam is indicated in the lower left corner of panel *d*.

gradient is resolved by our observations, in the sense that the position of the filament (which can be determined to a fraction of the beam width) is a systematic function of velocity. Furthermore, it is monotonic along the whole feature, with the velocity appearing to be a function of the distance from IRS 5. Below we investigate the possibility that the CO filaments could be shocks by comparing the physical properties of this feature with current theoretical models.

4.2. *The CO Filaments as Shocks*

Interstellar shocks may be divided into two classes according to whether the fluid velocities across the shock vary continuously or discontinuously. The former are the C (continuous)-shocks, whilst the latter are the J (jump)-shocks (Shull & Draine 1986). C-shocks occur in the presence of magnetic fields in a multicomponent fluid made up of neutral gas, ions, electrons, and charged grains and are therefore also termed as magnetohydrodynamic, or MHD, shocks. Other distinguishing characteristics of C-shocks are supersonic flow everywhere and a broader spatial extent (by as much as a factor of ~ 5), and lower peak temperature than found in corresponding J-shocks.

The deconvolved FWHM of the brightest CO feature (Figs. 3 and 4) varies between 5″.4 and 11″.0, corresponding to 1–2 $\times$ 10^{16} cm at 140 pc. For comparison, the characteristic widths of C-type shocks are 0.5–6.5 $\times$ 10^{16} cm for a wide range of preshock densities ($10^2 \leq n_H \leq 10^6$ cm^{-3}), ionization fractions ($10^{-4} \leq \chi_e \leq 10^{-8}$), and magnetic field strengths (10 μG $\leq B_0 \leq$ 1.0 mG) and assuming a 25 km s^{-1} shock velocity (Draine, Roberge, & Dalgarno 1983 [DRD]). From the combination of a resolved velocity gradient across the filament, its width, and detection of supersonic velocities throughout, we suggest that the emission region is a C-type shock. Furthermore, the sense of the observed velocity gradient is exactly what would be expected for blueshifted gas from IRS 5 interacting with, and being slowed by, the ambient cloud material. The relatively low observed maximum radial velocity, $v_{r,\max}$, could be explained as due to orientation effects: a higher, true shock velocity, v_s, being viewed at an angle $v_{r,\max} = v_s \cos i$. For a 25 km s^{-1} shock, this viewing angle would be $\approx 73°$ in our case. According to models of C-shocks (DRD), an ambient magnetic field of 10–30 μG would suffice to produce the observed shock structure.

C-type shocks can be further broken down into two classes: C-type, characterized by relatively low Mach numbers ($M < 5$) and C*-type, characterized by high Mach numbers ($M \geq 18$) (Roberge & Draine 1990 [RD]; Smith & Brand 1990a). Representative velocity and temperature profiles across C-shocks and C*-shocks have been calculated by DRD and RD, respectively. The major distinguishing feature between a C-shock and a C* shock observationally, for the nearly identical preshock conditions and shock velocities, is the maximum temperature attained by the neutral gas. For similar input parameters, $T_{n,\max} = 1223$ K for a C-type shock, whereas $T_{n,\max} = 6474$ K in the C*-type shock (DRD and RD, respectively).

A determination of the temperature structure across this MHD shock front requires high spatial resolution mapping of appropriate near-infrared emission lines. Comparison of near-infrared shock-excited molecular line intensity ratios can give information about both the temperature and the density varia-

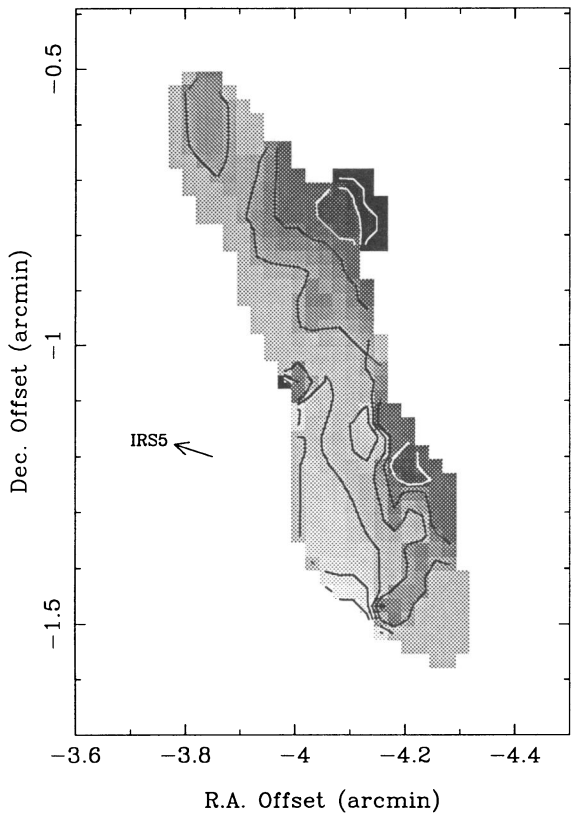

FIG. 4.—Velocity structure of CO (1–0) filament. First-moment map of the strongest CO emission feature detected by the interferometer, which shows the velocity structure across the filament. The gray scale and the contours depict the value of the LSR velocity, with lighter gray indicating the most blueshifted gas relative to the cloud rest velocity of V_{LSR} = 6.5 km s^{-1}, and darker gray indicating velocities progressively closer to the cloud rest velocity.The contours are spaced at 1 km s^{-1} intervals, starting at 1 km s^{-1} in the southeast to 8 km s^{-1} in the northwest.

tion in the neutral gas across the shock (Smith & Brand 1990b). For instance, the upper level of the $1 \rightarrow 0$ $S(1)$ (2.12 μm) line of H_2 is 7000 K above ground, whereas that of the CO $P(8)$ line (4.74 μm) is 3000 K above ground. Since this line ratio is a very sensitive probe of temperatures in the range expected for C* shocks, high spatial resolution ($\lesssim 3''$) mapping of these lines across the shock front discovered via the interferometric CO $J = 1 \rightarrow 0$ observations could definitively distinguish whether this is a C-type or C*-type shock. The resultant temperature profiles across the shock could subsequently be used to constrain MHD models of this region.

Line emission from shock-excited CO at 4.7 μm has recently been detected and mapped near BN in Orion (Geballe & Garden 1990). For peak 1 in Orion, the CO $P(8)/H_2$ $S(1)$ line ratio is $\approx 1/16$ (Geballe & Garden 1990; Scoville et al. 1983). Recent measurements of the H_2 $S(1)$ line intensity near L1551/IRS 5 span a range 4–22 $\times$ 10^{-22} W cm^{-2} in a 2.″9 $\times$ 4.″3 rectangular aperture (Yamashita & Tamura 1992), suggesting corresponding CO $P(8)$ line intensities of 2.5 $\times$ 10^{-23} W cm^{-2}–1.4 $\times$ 10^{-22} W cm^{-2} in the same aperture at the same location, assuming similar shock conditions to Orion peak 1. Of course, the shock conditions, the line-of-sight extinction, and the geometry may differ between Orion peak 1 and the L1551 shocks, so the above is just an order of magnitude estimate for the possible strengths of the CO $P(8)$ line emission from the vicinity of L1551/IRS 5. However, from this estimate it is clear that the determination of the temperature profile of the neutrals across the MHD shock detected by our OVRO observations, although difficult, would at least be feasible.

5. CONCLUSIONS

We have mapped 20 1′ diameter positions in the blueshifted lobe of the L1551 molecular outflow with the OVRO interferometer at $\approx 7''$ (N–S) $\times$ 4″ (E–W) resolution in the CO $J = 1 \rightarrow 0$ line.

We find no detectable emission with the interferometer in regions of relatively weak or missing single-dish emission, suggesting that in these regions the single-dish flux is not due to beam dilution. The lack of interferometer emission in regions of weak single-dish emission is therefore due to the presence of extended, smooth emission regions, such as would be expected from a molecular gas shell, proposed by previous authors to explain the CO gas morphology (see Moriarty-Schieven & Snell 1988 and references therein).

We find filamentary structures at the positions of the strongest single-dish emission regions, which are morphologically reminiscent of H_2 shock structures found in other outflows (Bally & Lane 1990; Garden & Carlstrom 1992). The strongest emission structure in all of our mapped fields coincides with a region of high obscuration in the HH 102 nebula. This feature has a radial velocity gradient across it, ranging from blueshifted gas (-6 km s^{-1} relative to the cloud rest velocity) to gas at the cloud rest velocity of 6.5 km s^{-1} V_{LSR}.

The FWHM (1–2 $\times$ 10^{16} cm) and velocity gradient of this emission structure are consistent with the properties expected for the neutral gas component across a C-type MHD shock front (Draine 1980; DRD; RD). Since CO shock emission has recently been detected at 4.7 μm in Orion (Geballe & Garden 1990), we suggest future observations of this shock feature in the near-infrared transitions of CO in order to determine the temperature structure of the neutrals across the shock and to distinguish whether this feature is a C-type (Draine 1980) or a C*-type (RD) shock.

We would like to thank Gerald Moriarty-Schieven for providing us with his FCRAO single-dish data of the L1551 outflow both before and after publication. We thank John Graham for providing us with the negatives of his beautiful, large-field CCD image of the L1551 region. M. B. thanks Lee Mundy for instruction in mosaicking data within AIPS and Remo Tilanus for the masking technique used to produce Figures 1 and 2. Thanks to L. Chernin, D. Christoudoulou, S. Curiel, P. T. P. Ho, and J. M. Torrelles for helpful discussions. C. J. C. acknowledges the support of a SERC/NATO Fellowship. Funding for the OVRO interferometer has been provided by NSF grant AST-9016404.

REFERENCES

Bally, J., & Lane, A. P. 1990, in Astrophysics with Infrared Arrays (ASP Conf. Ser. 14) ed. R. Elston, 273
Bally, J., & Stark, A. A. 1983, ApJ, 266, L61
Barsony, M., Yun, M. S., & Stark, A. A. 1993, in preparation
Clark, F. O., Laureijs, R. J., Chliwicki, G., Zhang, C. Y., van Oosterom, W., & Kester, D. 1986, A&A, 168, L1

Draine, B. 1980, ApJ, 241, 1021
Draine, B. T., Roberge, W. G., & Dalgarno, A. 1983, ApJ, 264, 485 (DRD)
Edwards, S., Strom, S. E., Snell, R. L., Jarrett, T. H., Beichman, C. A., & Strom, K. M. 1986, ApJ, 307, L65
Fridlund, C. V. M., Sandqvist, Aa., Nordh, H. L., & Olofsson, G. 1989, A&A, 213, 310
Garden, R., Russell, A. P. G., & Burton, M. G. 1990, ApJ, 354, 232
Garden, R. P., & Carlstrom, J. E. 1992, ApJ, 392, 602
Geballe, T. R., & Garden, R. P. 1990, ApJ, 365, 602
Graham, J., & Heyer, M. H. 1990, PASP, 102, 972
Lizano, S., Heiles, C., Rodriguez, L. F., Koo, B.-C., Shu, F. H., Hasegawa, T., Hayashi, S., & Mirabel, I. F. 1988, ApJ, 328, 763
Moriarty-Schieven, G. H., & Snell, R. L. 1988, ApJ, 332, 364
Moriarty-Schieven, G. H., Snell, R. L., Strom, S. E., Schloerb, F. P., Strom, K. M., Grasdalen, G. L. 1987, ApJ, 319, 742
Rainey, R., White, G. J., Richardson, K. J., Griffin, M. J., Gronin, N. J., Monkiro, T. S., & Hilton, J. 1987, A&A, 179, 237
Roberge, W. G., & Draine, B. T. 1990, ApJ, 350, 700 (RD)
Rodriguez, L. F., Lizano, S., Cantó, J., Escalante, V., & Mirabel, I. F. 1990, ApJ, 365, 261
Russell, A. P. G., Bally, J., Padman, R., & Hills, R. E. 1992, ApJ, 387, 219
Scoville, N. Z., Hall, D. N. B., Kleinmann, S. G., & Ridgway, S. T. 1983, ApJ, 253, 136
Shull, J. M., & Draine, B. T. 1986, in Interstellar Processes, ed. D. J. Hollenbach & H. A. Thronson (Dordrecht: Reidel), 283
Smith, M. D., & Brand, P. W. J. L. 1990a, MNRAS, 242, 495
———. 1990b, MNRAS, 243, 498
Snell, R. L., Bally, J., Strom, S. E., & Strom, K. M. 1985, ApJ, 290, 587
Snell, R. L., Loren, R., & Plambeck, R. L. 1980, ApJ, 239, L17
Snell, R. L., & Schloerb, F. P. 1985, ApJ, 295, 490
Stark, A. A., Gammie, C. F., Wilson, R. W., Bally, J., Linke, R. A., Heiles, C., & Hurwitz, M. 1992, ApJ, 79, 77
Stocke, J. T., Hartigan, P. M., Strom, S. E., Strom, K. M., Anderson, E. R., Hartmann, L. W., & Kenyon, S. J. 1988, ApJ, 68, 229
Uchida, Y., Kaifu, N., Shibata K., Hayashi, S. S., Hasegawa, T., & Hamatake, H. 1987, PASJ, 39, 907
Yamashita, T., & Tamura, M. 1992, ApJ, 387, L93